Journal of Alloys and Compounds 766 (2018) 1014–1023

Contents lists available at ScienceDirect

Journal of Alloys and Compounds

journal homepage: http://www.elsevier.com/locate/jalcom

All inorganic based $Nd_{0.9}Mn_{0.1}FeO_3$ perovskite for Li-ion battery application: Synthesis, structural and morphological investigation

K.O. Ogunniran [a, b, *], G. Murugadoss [b], R. Thangamuthu [b], P. Periasamy [c]

[a] Department of Chemistry, College of Science and Technology, Covenant University, PMB, 1023, Ota, Ogun State, Nigeria
[b] Electrochemical Materials Science Division, CSIR-Central Electrochemical Research Institute, Karaikudi, 630 003, Tamil Nadu, India
[c] Electrochemical Power Sources Division, CSIR-Central Electrochemical Research Institute, Karaikudi, 630 003, Tamil Nadu, India

ARTICLE INFO

Article history:
Received 14 February 2018
Received in revised form
16 June 2018
Accepted 27 June 2018
Available online 30 June 2018

Keywords:
Cyclic voltammetry
Li-ion battery
Nanostructures
X-ray diffraction
Structural morphology
X-ray photoelectron spectroscopy

ABSTRACT

Mn doped perovskite structured $Nd_{0.9}Mn_{0.1}FeO_3$ nanoparticles have been successfully prepared using hydrothermal method in aqueous medium. The structural and morphological properties were investigated using XRD, SEM, FE-SEM, and TGA. After establishing the structure and morphology of the compound, thorough investigation into elemental composition with the use of EDX and XPS were carried out. Microstructure arrangement was done with the use of HR-TEM while the BET analysis confirmed the high surface area of the nanoparticles. The structural information was further investigated by AFM. The average particle size of $Nd_{0.9}Mn_{0.1}FeO_3$ nanoparticles increased from 60 to 100 nm with increasing annealing temperature from 500 to 1000 °C, respectively. The structural characterizations confirmed the perovskite nanoparticles to be crystalline orthorhombic structure. Moreover, the new material was explored as anode material for Li-ion battery. The galvanostatic cycling measurement shows that the cells possess reversible specific capacity of 763 $mAhg^{-1}$ at a current density of 0.5 A g^{-1} after 100 cycles. The charging and discharging profiles shows that the compound of this kind could be future candidate for electrode material.

© 2018 Elsevier B.V. All rights reserved.

1. Introduction

The demand for renewable energy in electricity production and transportation sector is increasing rapidly everyday over the last decade due to steady increase in the world population [1–3]. Also, due to dwindling resources and uncontrolled environmental pollution issues, the ease of processing the fossil fuel to cater for urgent demands has reduced drastically [4,5]. In order to meet up with these challenges, researchers have been directing efforts toward controlling the situation by seeking new and efficient ways to produce, transport, store, and consume energy [6–9]. High demand for better technology on energy storage and conversion has brought innovation to rechargeable batteries with design of new electrodes to improve their cycling life [7,10–13]. Based on this idea, Lithium ion (Li-ion) batteries have experienced continuous development in the last decades [12,14–18]. The new generation of energy technology is gearing towards designing super specific electrodes for lithium ion batteries with high safety performance [10,11], high energy and power density to exhibit a higher theoretical specific capacity which will be much higher than that of the present commercial electrode materials in the market [19–21]. It has been reported [15,17,22,23] that Li-ion batteries possess higher energy density than other common batteries such as lead acid, Nickel Cadmium (Ni-Cd) and Nickel Metal Hydroxide (Ni-MH) used in various applications. Therefore, it has attracted much interest from both industries and governments. The lithiated graphite anode has been reported to have maximum gravimetric capacity of 372 mAg^{-1} [6,24–26]. The future must be shaped to guarantee continuous sustainable of Li-ion batteries by developing new anode materials that allow Li-based batteries to have high gravimetric and volumetric capacity and power density as the current graphite anodes material can hardly meet the future demand for high energy.

In the quest for new anode materials, transition metal oxides and alloys have been extensively explored by various research groups within the current decades. The GeO_2 and Ge/C composite have been reported to show high capacities of 1860 and

* Corresponding author. Department of Chemistry, College of Science and Technology, Covenant University, PMB, 1023, Ota, Ogun State, Nigeria.
E-mail address: kehinde.ogunniran@covenantuniversity.edu.ng (K.O. Ogunniran).

https://doi.org/10.1016/j.jallcom.2018.06.340
0925-8388/© 2018 Elsevier B.V. All rights reserved.

1680 $mAhg^{-1}$ coupling with good cycling stability, at the current rates of 1C and 10C, respectively while ferrites like Fe_3O_4/RGO, and $CuFe_2O_4$ have been displayed as promising anode materials with high specific capacity of around 849.6 $mAhg^{-1}$ and 670 $mAhg^{-1}$ accordingly [27–29]. However, studies show that 3D materials get confronted with reduce voltage hysteresis at higher temperature.

Metal oxide based ABO_3 perovskite materials have been exploited for various area of applications such as catalytic applications [30,31], sensors, permeation membranes [32], photo electrolysis of water producing hydrogen, magnetic data storage, solid oxide fuel cells [33–35], glass-polishing [36], and as an ultraviolet absorbent in photovoltaic applications [37–40]. It is a material with great flexibility and has been adopted successfully as anode material in Ni/MH batteries due to its thermal stability [41,42] ease of preparation and it ability to tune its properties to fit the current system. They have high proton conductivity at high temperatures than other metal oxides [43]. Exploring perovskites type oxide as anode material in Li-ion batteries is a research area under development. Thus, the idea leads us to designing of new perovskite material with special combination arrangement which may involve doping of A or B site to enhance its electronic and optical properties. Several routes have been used to prepare perovskites, includes chemical methods, such as sol–gel [45–47], pyrolysis of metallo-organic precursors, combined polymerization, co-precipitation and hydrothermal routes [48–50]. Among these methods, hydrothermal method has been found to be a simple and gives room to structural modification to obtain the desired morphology [51,52].

Herein, we explore Mn doped $Nd_{0.9}Mn_{0.1}FeO_3$ perovskite as the anode material for the first time in our quest for new anode material with high specific capacity to replace the commonly used graphite anode. The perovskite was prepared through facile hydrothermal method and structurally established to confirm the presence of manganese within its distorted octahedral structure. This is expected to significantly increase the electronic conduction of the material and hence should not significantly vary as Li is intercalated and de-intercalated within the Li-ion batteries.

2. Experimental

2.1. Materials preparation

Neodymium nitrate hexahydrate ($Nd(NO_3)_3.6H_2O$), manganese nitrate hexahydrate ($Mn(NO_3)_2.6H_2O$), iron (III) nitrate nonahydrate ($Fe(NO_3)_3.9H_2O$) and citric acid monohydrate ($C_6H_8O_7.H_2O$) were used as starting materials. All the chemicals used are products of Sigma-Aldrich. They are of analytical pure grade (99.9%) and used as obtained without further purification.

The nanostructure perovskite $Nd_{0.9}Mn_{0.1}FeO_3$was synthesized via hydrothermal method [36,37]. Briefly, equivalent of 0.9 M of neodymium nitrate hexahydrate (11.83 g) was dissolved in 20 mL of doubly distilled water and stirred for 30 min after which solutions of 0.1 M (0.75 g) of manganese nitrate hexahydrate and 1 M (12.12 g) of iron (III) nitrate nonahydrate in 30 mL of distilled water were added and further stirred for 30 min to obtain black solution. The molar amount of citric acid added as surfactant was equal to the total molar number of precursors in the solution. The solution was stir for 2 h before it was transferred into a 100 mL Teflon-lined stainless-steel autoclave, sealed and put in hot air oven. The temperature was maintained at 180 °C for 24 h after that the autoclave was removed from the oven and allowed to cool to room temperature. The precipitate obtained was separated with centrifugation, washed with deionized water, anhydrous ethanol several times respectively and then dried in air at 100 °C for 4 h. The powder product obtained was calcined different temperatures at 400 500, 700 and 900 °C for 5 h each with the heating rate set at 5 °C min^{-1} to obtain maximum open porosity using programmed box furnace. The product obtained at the end of each step of the calcination was subjected to characterization.

2.2. Characterization

Thermogravimetric analysis was performed using simultaneous thermal analyzer (TG/DTA, SDT Q 600 V20) within the range of RT to 1000 °C under nitrogen atmosphere. Powder X-ray diffraction (XRD) was carried out in a PANalytical X'Pert PRO X-ray diffractometer with Cu-Ka radiation at a scanning rate of 0.02°s^{-1}. Fourier transform infrared (FT-IR) spectroscopy was performed on a Thermo Nicolet 200 FT-IR spectrometer using the KBr pellet technique. A spectrum was collected in the mid-IR range from 400 to 4000 cm^{-1} with a resolution of 1 cm^{-1}. The surface morphology, chemical composition, and structural identification of the prepared material were characterized with the use of Field Emission Scanning Electron Microscopy (FE-SEM), energy-dispersive X-ray analysis (EDX) (SEM - JEOL JSM-6380LV), and high-resolution transmission electron microscopy (HRTEM, JEM 2100 F), performed with an acceleration voltage of 200 kV by placing the powder on a copper grid. The selected area electron diffraction (SAED) patterns were also obtained by HR-TEM and were interpreted with the use of CrysTBox software. X-Ray photoelectron spectroscopy (XPS) measurements were obtained using the ESCA + Omicron UK XPS system with a Mg-Ka source and photon energy of 1486.6 eV. All the binding energies were referenced to the C 1s peak at 284.6 eV of the surface adventitious carbon. The Brunauer Emmett-Teller (BET) isotherm of the product calcined at 900 °C was analysed by nitrogen adsorption in a Autosorb iQ station 1 (version 3.01) adsorption apparatus. The sample was degassed at 180 °C prior to nitrogen adsorption measurements. Desorption and adsorption isotherms were used to determine the pore size distribution and surface area by the Barret–Joyner–Halender (BJH) method.

2.3. Electrochemical measurements

The electrochemical measurements of the product calcined at 900 °C were recorded using 2032-coin cells. Working electrodes consist of active material (70 wt %), acetylene black (20 wt%) and polyvinylidene fluoride binder (10 wt %) dissolved in N-methyl-2-pyrrolidone grounded to form homogeneous slurries and paste onto pure Cu foil followed by vacuum dried at 70 °C for 24 h. The coated Cu foil was punched into disks and used as the working electrodes. The cells were assembled in an Ar-filled glovebox (O_2 and H_2O contents <1 ppm) using lithium metal as the counter/reference electrode while celgard 2400 polypropylene film was used as the separator. The electrolyte used is 1 M LiPF6 dissolved in a mixture of ethylene carbonate, dimethyl carbonate, and diethyl carbonate (1:1:1, in vol. %). The electrochemical performances of the cells were evaluated by galvanostatic charge/discharge (GCD) on a Land CT 2001A battery tester within the voltage range of 0.02–3 V (vs. Li/Li^+). Cyclic voltammetry (CV) was conducted on a CHI-660D electrochemical workstation with a scan rate of 0.5 mV s^{-1} within a voltage window of 0.02–3 V (vs. Li/Li^+). Electrochemical impedance spectroscopy (EIS) was performed within a frequency range of 100 kHz to 0.01 Hz by applying a sine wave with amplitude of 5 mV.

3. Results and discussion

3.1. Synthesis

The synthetic procedure followed is depicted in Fig. 1. The reaction paths leading to formation of nanoporous $Nd_{0.9}Mn_{0.1}FeO_3$

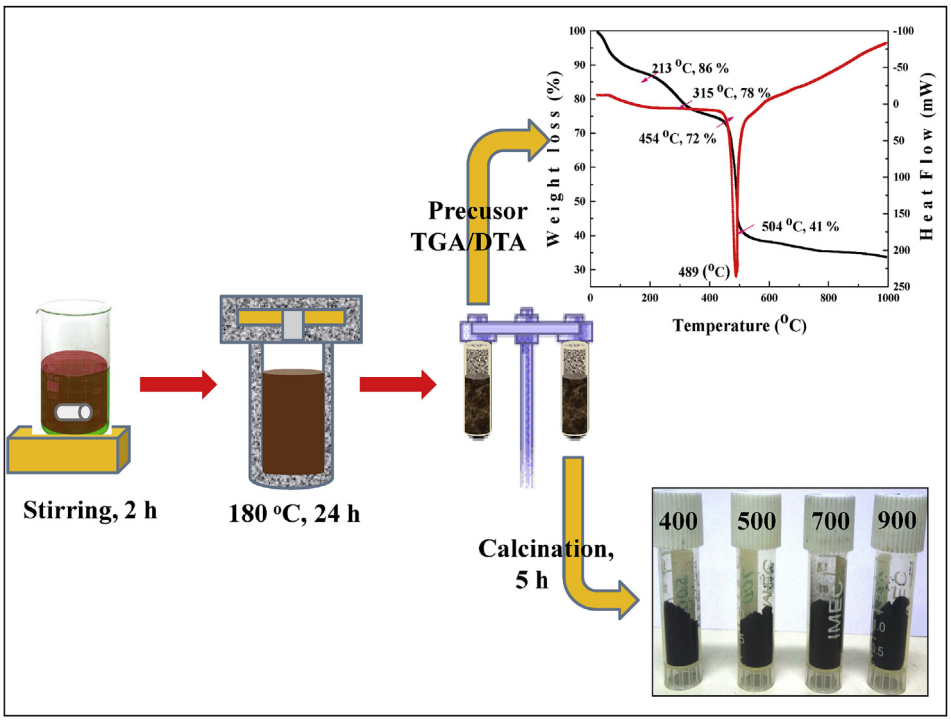

Fig. 1. Schematic diagram for the synthetic procedure of the nanoporous $Nd_{0.9}Mn_{0.1}FeO_3$, the photograph of the material obtained at different temperature and TGA/DTA curves for $Nd_{0.9}Mn_{0.1}FeO_3$ precursor from 25 to 1000 °C are presented together.

was carefully monitor with effect of gradual calcination temperatures increments which were proposed as follow:

$$0.9Nd(NO_3)_3\cdot 6H_2O \rightarrow 0.9Nd^{3+} + 2.7NO_3^- + 5.4H_2O \quad (1)$$

$$Fe(NO_3)_3\cdot 9H_2O \rightarrow Fe^{3+} + 3NO_3^- + 9H_2O \quad (2)$$

$$0.1Mn(NO_3)_2\cdot 9H_2O \rightarrow 0.1Mn^{2+}0.1NO_3^- + 0.9H_2O \quad (3)$$

$$0.9Nd^{3+} + 2.7OH^- \rightarrow 0.9Nd(OH)_{2.7} \quad (4)$$

The precursors obtained after centrifugation gives the TGA/DTA curves (Fig. 1) recorded within the temperature range of 25–1000 °C at heating rate of 10 °C/min. The precursors decomposed in four major steps with initial weight loss of 14% up to 213 °C which was attributed to the loss of absorbed and lattice water molecules in the precursor. Decomposition and transformation of citric acid to FeOOH, which processed to Fe_2O_3, occurred between 213-315 and 315–454 °C with 4 and 6% decomposition, respectively [38, 39]. Major weight loss of about 31% attributed to unreacted species (residual hydroxyl groups) which decomposed to form crystalline phase of $Nd_{0.9}Mn_{0.1}FeO_3$ was observed between 454 and 489 °C. The TGA/DTA analysis revealed the pure crystalline phase formation for $Nd_{0.9}Mn_{0.1}FeO_3$ to be ~500 °C.

$$Fe^{3+} + Mn^{2+} + C_6H_8O_7 + xH_2O \longrightarrow \sim\sim 0.1Mn^{2+}\text{-----}C_6H_8O_7\text{-----}Fe^{3+}\sim\sim \quad (5)$$

$$0.9Nd(OH)_{2.7} + \sim\sim C_6H_8O_7\text{------}0.1Mn^{2+}\text{--------}C_6H_8O_7\text{-------}Fe^{3+}\text{-------}C_6H_8O_7\sim\sim \longrightarrow Nd_{0.9}Mn_{0.1}FeO_3\downarrow + xC_6H_8O_7 \quad (6)$$

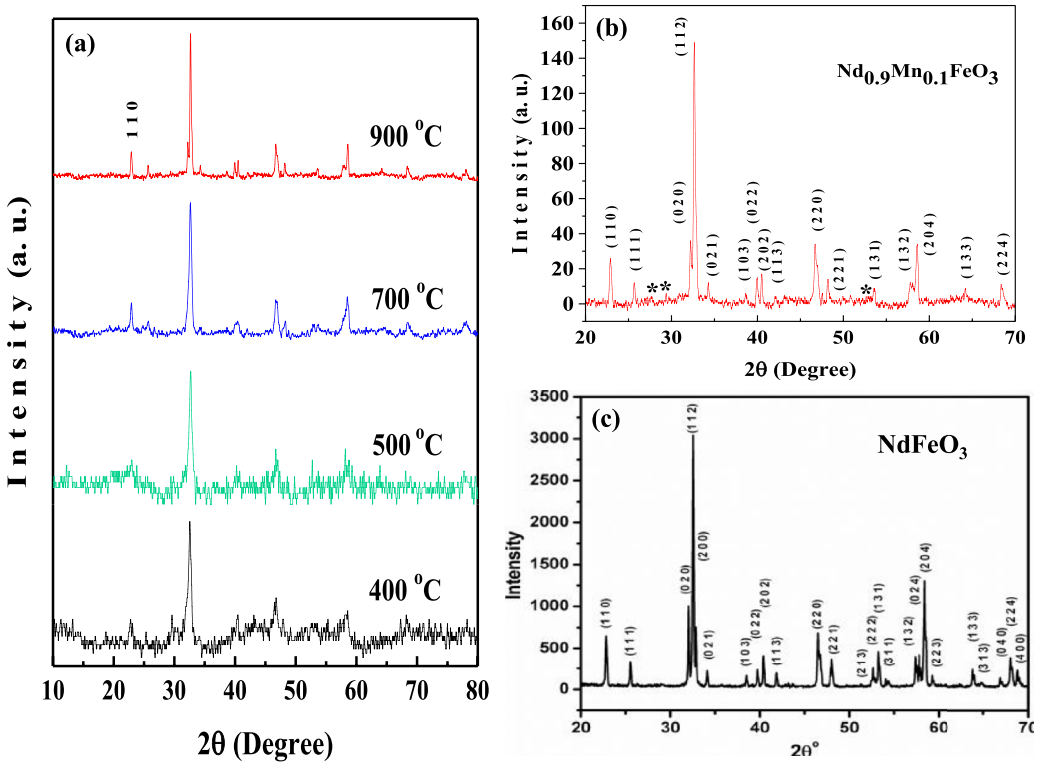

Fig. 2. (a) XRD patterns of $Nd_{0.9}Mn_{0.1}FeO_3$ calcined at 400, 500, 700 and 900 °C revealing pure crystalline phase formation as temperature increases. (b) Indexed XRD pattern of $Nd_{0.9}Mn_{0.1}FeO_3$ nanoporous $Nd_{0.9}Mn_{0.1}FeO_3$ calcined at 900 °C from 20 to 70° (c) XRD pattern of $NdFeO_3$ nanopowder from 20 to 70°, Copyright: Journal of Applied Physics, 2012 [57].

3.2. XRD analysis

The typical XRD patterns of each of the products calcined at 400, 500, 700 and 900 °C are shown in Fig. 2a. The gradual increase in calcination temperature from 400 to 900 °C is to study structural changes leading to pure crystalline phase formation. The 400 °C was selected as the starting point calcinations based on the result of the TGA/DTA analysis. XRD patterns for the product calcined at 500 °C confirmed that the products are partly amorphous due to lack of pure crystalline phase. However, XRD patterns of the product calcined at 700 and 900 °C displayed pure crystalline phase with strong characteristic peaks at 22.97 and 33.65°attributable to those of the standard pattern and all the detectable peaks in the patterns can be readily indexed to a pure orthorhombic phase (space group: *Pnma*) with lattice constants a = 5.4840 Å, b = 7.5812 Å, c = 4.9542 Å (JCPDS 88-477). The temperature variation gives ample opportunity to follow the effect of temperature on structural orientation as the reaction progresses within the compound. The indexed XRD pattern of $Nd_{0.9}Mn_{0.1}FeO_3$ is shown in Fig. 2b. The indexed peaks were also compared with literature $NdFeO_3$ indexed peaks (Fig. 2c) and shows major crystalline planes corresponded to (110), (111), (020), (112), (021), (022), (202), (220), (204) and (224). Slight variation observed is expected due to distortion of A side of the perovskite because of the presence of Mn^{2+} ion within the octahedral structure of Nd^{3+} ion in the perovskite. No new peaks were observed except reduction in intensity of some of the $NdFeO_3$ peaks due to effect of distortion of Mn^{2+} ion. Well visible intensity of the detected peaks supports the purity of the compound with good crystallinity [42,43].

3.3. FT-IR analysis

As functional group identification tool, Fourier transform infrared (FT-IR) spectroscopy was used to monitor the reaction progress at each stage of calcinations. The CO, NO, OH and M-O chromophoric groups vibrational bands were used to affirm the crystalline phase formation as calcination temperature increase. Fig. S1 (supplementary data 1) shows the FT-IR results of the perovskites at different calcination temperatures. The spectrum at 400 °C shows band at 3434, 1499-1381and 572 cm^{-1} assigned to OH, CO and M-O vibrational stretching band of the surfactant and metal oxide respectively [45]. The spectrum at 500 °C shows strong C═O symmetric and asymmetric vibration stretching bands with reduced OH vibrational band intensity. This is an indication that $Fe(OH)_3$ have decomposed to Fe_2O_3 in the precursor. The spectrum at 700 °C displays weak OH absorption band with complete volatilization of CO vibrational band to have partial crystalline phase formation at this temperature. Pure phase formation was recorded at 900 °C with appearance of only absorption band related to M-O at 569 cm^{-1}. The spectra obtained are like the FT-IR of $NdFeO_3$ earlier reported in the literatures. Thus, it can be concluded that pure crystalline phase formation occurred at 900 °C.

3.4. Morphological studies

The morphological investigation of $Nd_{0.9}Mn_{0.1}FeO_3$ nanoparticles was used to follow up structural changes that lead to crystalline phase formation as the calcinations temperature increases. Fig. 3a-c shows the images SEM of product calcined at 400,

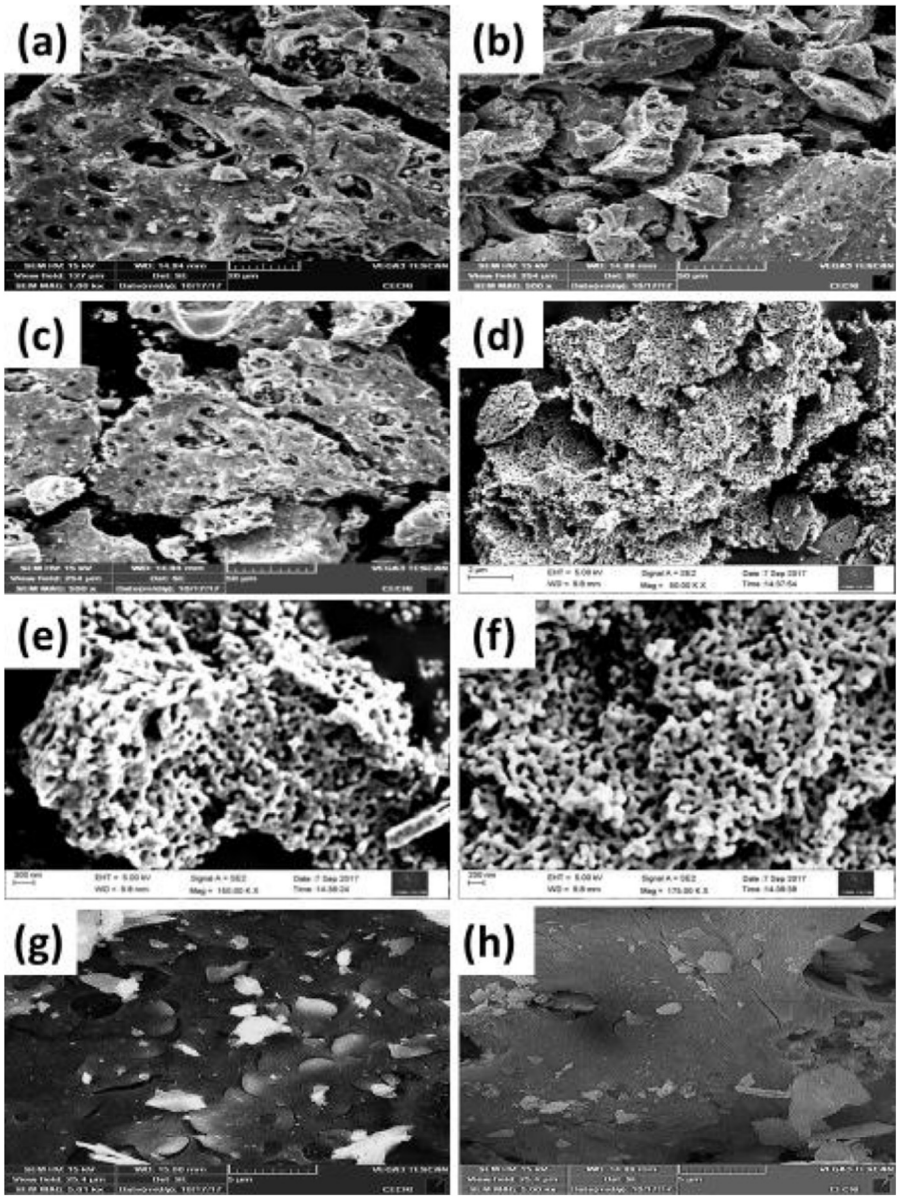

Fig. 3. (a–c) SEM images of $Nd_{0.9}Mn_{0.1}FeO_3$ nanoparticles calcined at 400, 500 and 700 °C at different magnifications revealing gradual structural formation pure nanoporous morphology of the perovskite. (d–f) FE-SEM images of $Nd_{0.9}Mn_{0.1}FeO_3$ nanoparticles calcined at 900 °C at 2 μm, 200 nm and 300 nm magnifications, respectively.

500 and 700 °C respectively, while Fig. 3d-f shows the FE-SEM images of the product calcined at 900 °C. For comparison, SEM images of undoped sample calcined at 900 °C is shown in Fig. 3 (g, h). SEM morphology study reveals the structure at 400 °C to be highly porous cavity with the presence of loosely packed amorphous material that could be traced to the presence of surfactant and doped Mn, as confirmed by FT-IR, in the product. The morphology obtained from the product calcined at 500 °C shows that the material has been reoriented to form lumps of porous material with presence of trace quantity of surfactant in the system while the dopant (Mn) allied with the phase formation of the perovskite. Pure lump of porous particle appears at 700 °C. The pure crystalline phase with symmetrical nanoporous material was observed at 900 °C. The new $Nd_{0.9}Mn_{0.1}FeO_3$ nanoparticles possess regular pore sizes and are packed together without the trace of surfactant. The morphology obtained from FE-SEM reveals the role of surfactant as mere structural orientation agent as the temperature increases and aids in bond breaking, bond rearrangement bond formation within the material cavity. The gradual increase in the temperature coupled with the effect of dopant (Mn) could be the factors that contributed greatly to the formation of porosity in the perovskite. This is evidenced with the formation of homogeneous agglomerates crystalline nanomaterial for $NdFeO_3$ (Fig. 3g and h) in the absence of Mn as obtained in the previous studies [44].

The HR-TEM images at different magnifications with selected area electron diffraction pattern (SAED) are presented in Fig. 4a–b for further insight into the morphology of $Nd_{0.9}Mn_{0.1}FeO_3$ nanoparticles at micro-structure level. Fig. 4a shows uniform fringes image showing light and dark area of pure crystalline phases of the perovskite. The image in Fig. 4b reveals the uniform fringes with interplanar arrangement of the nanoparticles in the perovskite. The interplanar spacing layer was measured using CrysTBox software to be within the average of 0.244 nm which was indexed in the XRD pattern to be *d*-spacing of 112 plane of the orthorhombic crystal structure. The right inset is the picture of unit cell of the perovskite showing the interplanar d-spacing arrangement which supported

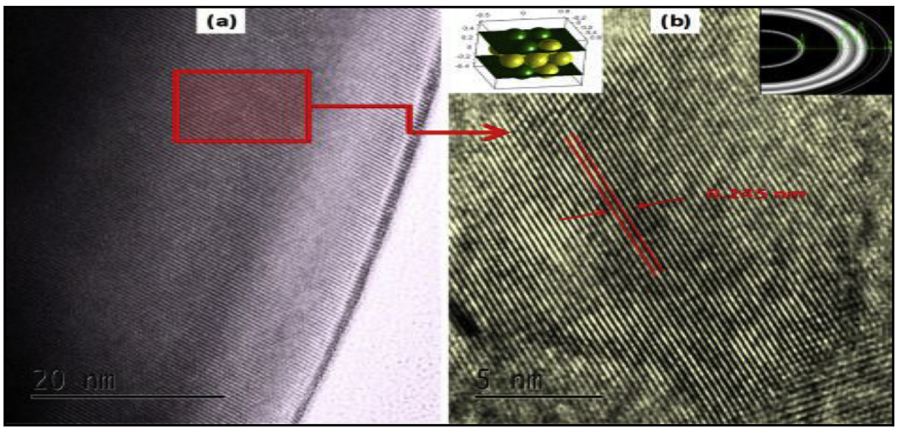

Fig. 4. HR-TEM images of $Nd_{0.9}Mn_{0.1}FeO_3$ nanoparticles calcined at 900 °C with different magnifications (a) lattice fringes of $Nd_{0.9}Mn_{0.1}FeO_3$ crystallite with scale bar represents 20 nm. (b) Magnified image of the fringes with 5 nm scale of the perovskite inset pictures showed the unit cell with the SASED pattern.

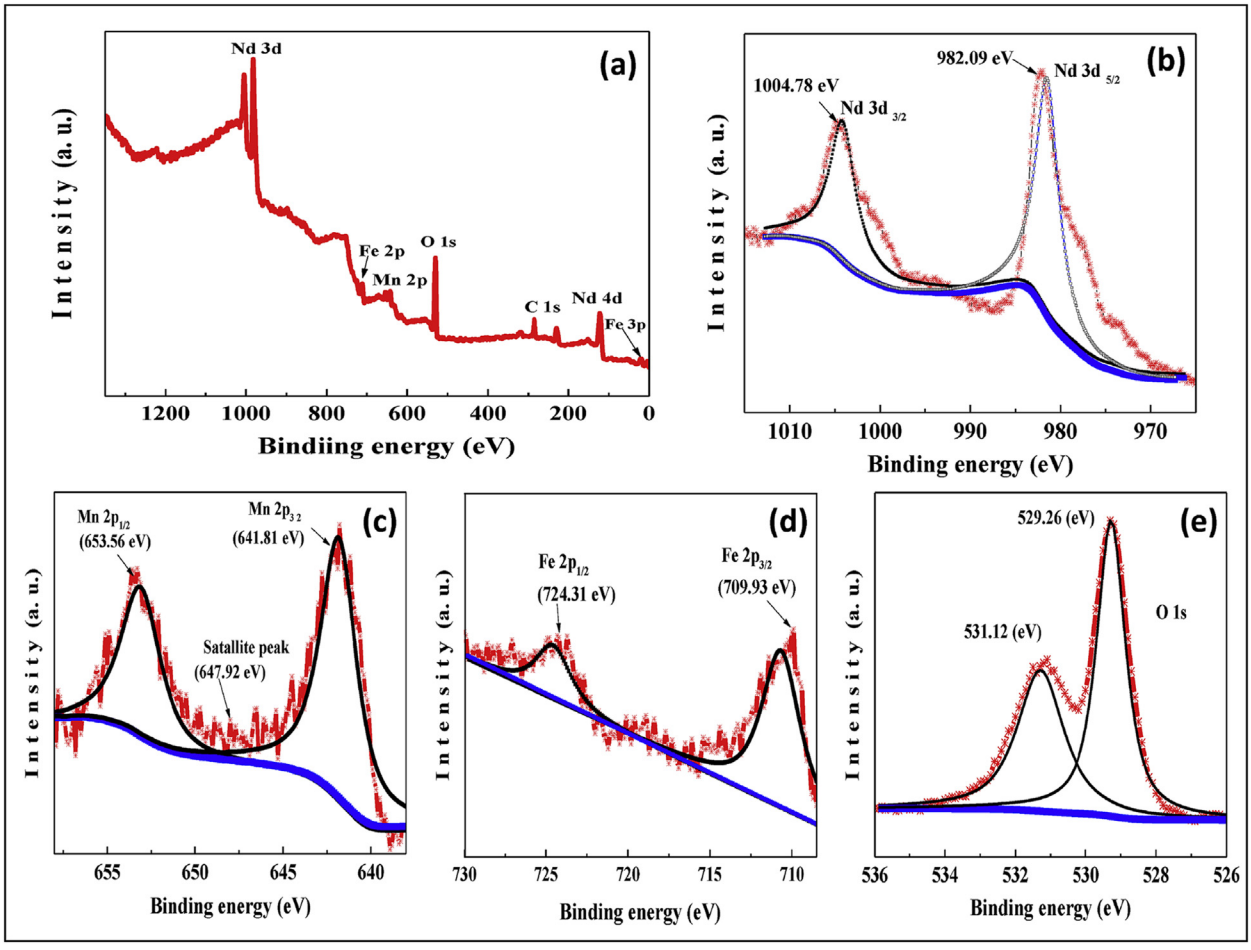

Fig. 5. Surface elemental composition of the samples. (a) High-resolution XPS survey spectrum of $Nd_{0.9}Mn_{0.1}FeO_3$ nanoparticle calcined at 900 °C. Core level spectrum scan for (b) Nd 3d, (c) Mn 2p, (d) Fe 3p and (e) O 1s.

orthorhombic crystal structure lattice as deduced by XRD. Also, the crystallites diffraction pattern (left inset) shows the diffractogram which could be related to XRD pattern obtained for the perovskite at 900 °C. The crystallites diffraction pattern image confirms regular arrangement of the particles in the perovskite and thereby possess high tendency of crystalline nature. The presence of crystalline particles supports the purity of the compound.

3.5. Elemental (EDX and XPS) analyses

The elemental composition of nanoporous $Nd_{0.9}Mn_{0.1}FeO_3$ was established with the use of EDX analysis. Fig. S2a shows the result of the EDS analysis obtained for $Nd_{0.9}Mn_{0.1}FeO_3$ annealed at 900 °C. The theoretical values were calculated based on molecular weight of the designed perovskite. The experimental values obtained from

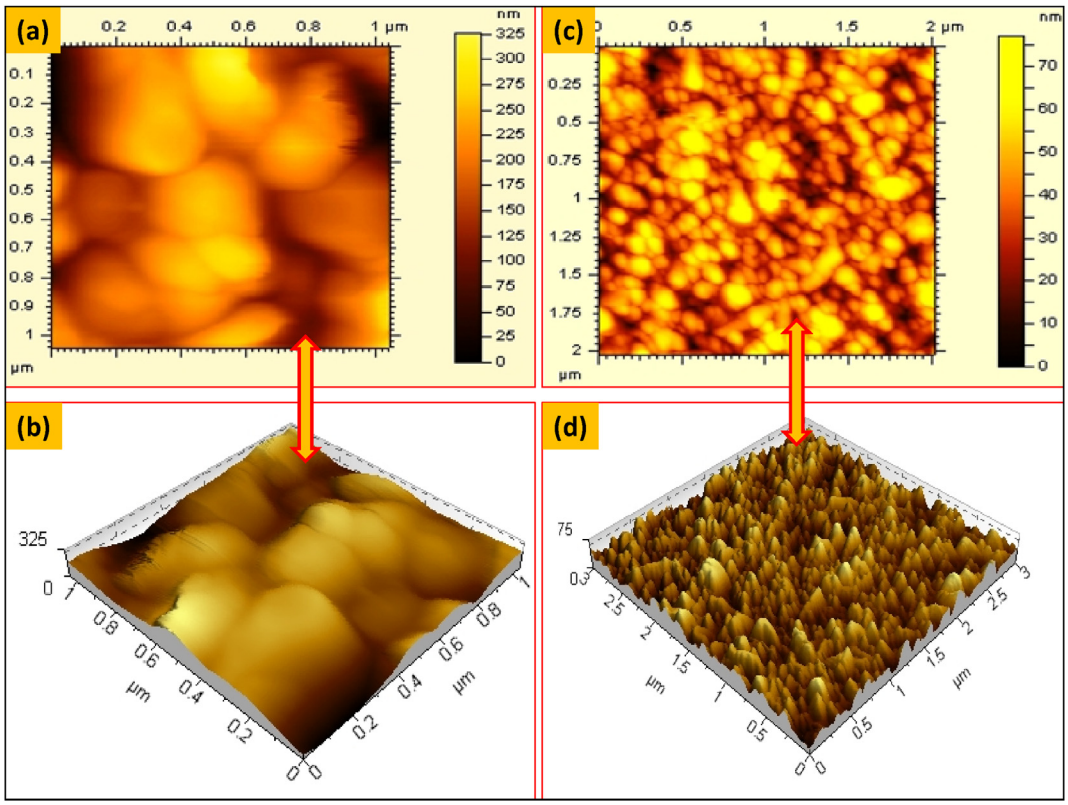

Fig. 6. AFM images of $Nd_{0.9}Mn_{0.1}FeO_3$ nanoporous calcined at 900 °C measured at different magnifications which spin coated on the FTO substrate.

EDX analysis correlated with the theoretical values within the experimental error of ±2. For more clarity, the result is presented in bar chart form in Fig. S2b. Thus, EDX result reveals the composition elements Nd/Mn/Fe/O in the perovskite to be in ratio 0.9:0.1:1:3.

Confirmation of the oxidation state of the composition elements of the nanoparticles of $Nd_{0.9}Mn_{0.1}FeO_3$ was done with the use of X-ray photoelectron spectroscopy (XPS). Fig. 5a-e shows the XPS spectra of the nanoparticles of $Nd_{0.9}Mn_{0.1}FeO_3$ calcined at 900 °C. The survey scan of the sample (Fig. 5a) shows the peaks attributed to binding energy of Nd, Mn, Fe and O [38,52]. However, the peak observed at 285 eV could be attributed to the carbon deposited from calcination environment. Fig. 5b shows core level peaks of Nd 3d attributed to $Nd_{3/2}$ and $Nd_{5/2}$ peaks in 3 + oxidation state at 1004 and 982 eV, respectively. The peaks at 653 and 641 eV (Fig. 5c) reveals the presence of core Mn $2p_{1/2}$ and Mn $2p_{3/2}$ with the appearance of satellite peak at 647 eV to confirm the presence of Mn^{2+} in the nanoparticle. Fig. 5d shows Fe 2p core binding energy peaks at 724 and 709 eV which is correlated to Fe $2p_{1/2}$ and Fe $2p_{3/2}$ peaks of Fe^{3+}, respectively. The wide and asymmetric peaks with high-resolution at binding energies of 530.1 and 528.1 eV was attributed to O 1s core peaks (Fig. 5e). The spectra fitted into two types of chemical states by Gaussian rule [53]. The absence of chemisorbed oxygen to form hydroxyl oxygen was confirmed with less than 2–2.5 eV difference between the peaks binding energies. Thus, we successfully achieved pure crystalline form of the nanoporous $Nd_{0.9}Mn_{0.1}FeO_3$ perovskite doped with Mn^{2+} at 900 °C as we proposed.

3.6. AFM analysis

Fig. 6 shows 2D and 3D atomic force microscopy (AFM) images of thin films of $Nd_{0.9}Mn_{0.1}FeO_3$ (calcined at 900 °C) deposited on the FTO substrate at 120 °C temperature.

The AFM images obtained at different magnifications reveal a packed uniform surface roughness with peaks height ranging 12–17 nm. The perovskite shows good adherence to the substrate with narrow particle size distribution indicating the ease of formation of the crystallites within the particles. The RMS value for deviation from the roughness profile is about 8.23 nm. The shape and size of the grains shows symmetrical and coherent as shown in the figure. This suggests increase rate of nucleation and the crystallization form crystallites as observed in the XRD and HR-TEM analysis.

3.7. Surface area analysis

The results of the surface area and pore volume analysis carried out by using automated surface area analyzer from nitrogen adsorption–desorption isotherms through BET and BJH methods for $Nd_{0.9}Mn_{0.1}FeO_3$ perovskite nanoparticles are shown in Fig. 7a-e. It shows that nanoparticles have broader pore size distribution. The isotherm results (Fig. 7a) show that nanostructure exhibit a type-D isotherm. This is a typical of lamella structure with large number of pores within high-pressure range of $0.07 < P/P0 < 0.97$. The wide ranges of partial pressure demonstrated the pore condensation of nitrogen molecule during adsorption which generated H3 type of hysteresis [54]. The BET analysis recorded the nanoparticle surface area to be 17.07 m^2/g. Also, Barrett–Joyner–Halenda (BJH) analysis results (Fig. 7b–e) obtained from adsorption and desorption area by correlating the cumulative pore volume (Fig. 7b and c) and cumulative surface area of the particles (Fig. 7e, d) to pore radius reveals the particle surface area to be 15.57 m^2/g. The pore volume (0.024 cc/g) and the pore radius Dv(r) (19.58 Å) were also determined. They were obtained from lower portion (20–100 Å) of pore

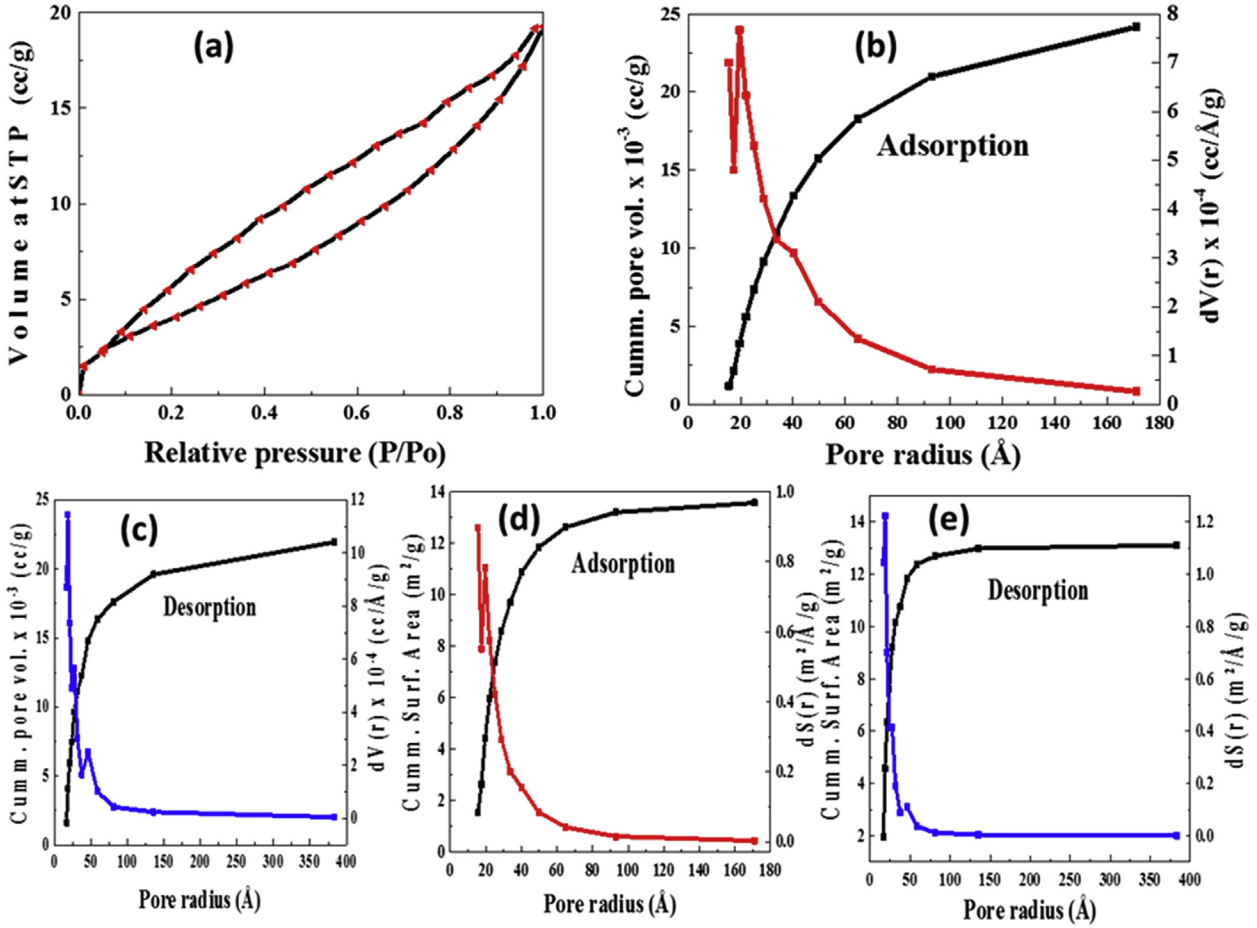

Fig. 7. (a) Nitrogen adsorption-desorption isotherms (b, c) BJH plot showing relative distribution of pore volume and pore radius from adsorption and desorption isotherm, (d, e) BJH plot showing relative distribution of surface area and pore radius from adsorption and desorption isotherm.

diameters in adsorption and desorption branch of the isotherm. The results confirmed the material to be relatively porous as supported by SEM analysis. However, the relatively large surface area of the nanoparticles and ability to coagulate into crystallites are unique characteristic of the material that could be explored in different area of applications.

3.8. Electrochemical studies

Fig. 8 (a) shows 1st - 8th charge-discharge profiles of $Nd_{0.9}Mn_{0.1}FeO_3$ electrode at a constant current of 0.5 A g^{-1}. The first cycle shows discharge capacity of 2550 mAhg^{-1} and charge capacity of 2400 mAhg^{-1} with columbic efficiency of 77%. The subsequent charge capacity reduced gradually until the charging capacity of about 763 mAhg^{-1} retained as shown in Fig. 8 (b). However, when the $Nd_{0.9}Mn_{0.1}FeO_3$ electrode is further cycled to 50 cycles, a high capacity of about 2200 mAhg^{-1} was maintained, suggesting that it has an extremely high Li storage property. To clarify the effect of the dopant (Mn) on the electrochemical property of $Nd_{0.9}Mn_{0.1}FeO_3$, the typical Nyquist plots that show semicircle and Warburg line monitored after charge-discharge cycles at 0.5 A g^{-1} is shown in Fig. 8c and d for $Nd_{0.9}Mn_{0.1}FeO_3$ and $NdFeO_3$ electrodes, respectively. Inset in Fig. 8c is the equivalent electrical circuit. The measurements were carried out on open circuit potential with AC voltage amplitude of 5.0 mV from 100 kHz to 0.01 Hz. The start of the semicircle is associated with the electrolyte resistance (*Rs*), the semicircle at high frequency corresponds to the charge transfer resistance (*Rct*) while the line near the end of the semicircle reveals the diffusion of lithium ions. Clearly, the medium range semicircle of $NdFeO_3$ electrode is much higher than that of $NdFeO_3$ electrode indicating larger charge-transfer resistance (*Rct*). The *Rct* values are 202 and 280 ohms for $Nd_{0.9}Mn_{0.1}FeO_3$ and $NdFeO_3$ electrodes, respectively. The low impedance value for $Nd_{0.9}Mn_{0.1}FeO_3$ nanoparticles indicates good reaction kinetics [55,56]. The presence of doped Mn ion in the electrode contributes to merging of nanoparticle surfaces which could enhance the electronic conductivity and thereby shorten the ionic/electronic transport length to give improved electrochemical performance.

4. Conclusion

In summary, we have successfully synthesized $Nd_{0.9}Mn_{0.1}FeO_3$ nanoparticles with the aim of improving its physical characteristics. The material has been successfully characterized to establish the molecular arrangements in perovskite structure. Doping with Mn has been observed to have effect on the nanosize arrangement of the particles thereby affecting the particles size and shapes. Hydrothermal method used has given ample opportunity to follow the molecular orientation at different temperature to get the final product. The structural and morphological information were studied with XRD, SEM and FE-SEM analyses. Elemental composition and ionic state of the composition were confirmed with XPS analysis. The deep knowledge into the micro atomic arrangement was resolved with the use of HR-TEM and AFM analysis. BET study

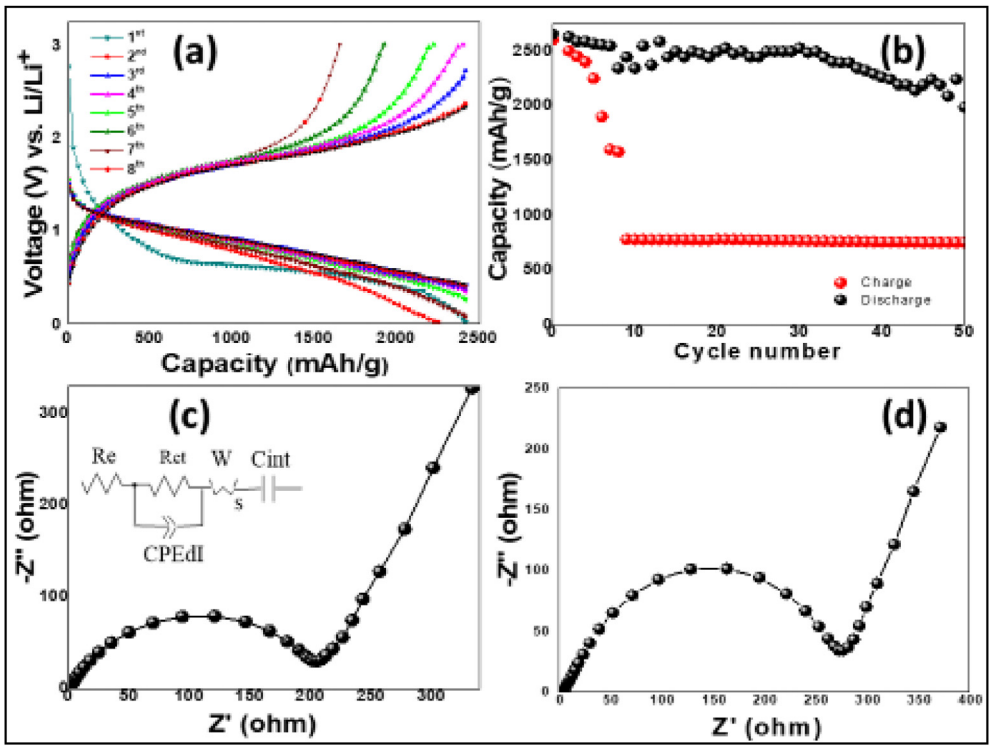

Fig. 8. (a) The 1st – 8th charge-discharge profiles of $Nd_{0.9}Mn_{0.1}FeO_3$ electrode between 0.02 and 3 V at a constant current of 0.5 A g^{-1}. (b) Cycling performance of $Nd_{0.9}Mn_{0.1}FeO_3$ electrode at a constant current of 0.5 A g^{-1}. Equivalent circuit and electrochemical impedance spectrum of $Nd_{0.9}Mn_{0.1}FeO_3$ (c) and $NdFeO_3$ (d) respectively.

confirmed the surface area and the pore sizes of the particles. Moreover, we have successfully explored the possibility of $Nd_{0.9}Mn_{0.1}FeO_3$ perovskite nanoparticles as electrode material for Li-ion battery. Even though there is limitation in our electrochemical studies; few results obtained proved that the material could successfully used as electrodes with good retention capacity of 760 mA h g^{-1}. Hence, this research opens insight into designing and exploring all inorganic based stable perovskites materials for battery application.

Acknowledgement

One of the authors, K. O. Ogunniran express his gratitude to CISR and TWAS for financial support through TWAS-CSIR postdoctoral fellowship grant to carry out this work. The authors thank Dr. Vijayamohanan K Pillai, Director, CSIR-Central Electrochemical Research Institute, Karaikudi, India for his constant support and encouragement. The authors also thank all the technical staff of CSIR-Central Electrochemical Research Institute for their support to carry out characterization studies.

Appendix A. Supplementary data

Supplementary data related to this article can be found at https://doi.org/10.1016/j.jallcom.2018.06.340.

References

[1] S. Sorrell, Reducing energy demand: a review of issues, challenges and approaches, Renew. Sustain. Energy Rev. 47 (2015) 74–82.
[2] M.Z. Jacobson, M.A. Delucchi, Providing all global energy with wind, water, and solar power, Part I: technologies, energy resources, quantities and areas of infrastructure, and materials, Energy Pol. 39 (3) (2011) 1154–1169.
[3] N.L. Panwar, S.C. Kaushik, S. Kothari, Role of renewable energy sources in environmental protection: a review, Renew. Sustain. Energy Rev. 15 (3) (2011) 1513–1524.
[4] M. Asif, T. Muneer, Energy supply, its demand and security issues for developed and emerging economies, Renew. Sustain. Energy Rev. 11 (7) (2007) 1388–1413.
[5] S.O. Oyedepo, On energy for sustainable development in Nigeria, Renew. Sustain. Energy Rev. 16 (2012) 2583–2598.
[6] N. Nitta, F. Wu, J.T. Lee, G. Yushin, Li-ion battery materials: present and future, Mater. Today 18 (5) (2015) 252–264.
[7] A. Sonoc, J. Jeswiet, V. KieSoo, Opportunities to improve recycling of automotive lithium ion batteries, Procedia CIRP 29 (2015) 752–757.
[8] R. Arvidsson, D. Kushnir, S. Molander, B.A. Sandén, Energy and resource use assessment of graphene as a substitute for indium tin oxide in transparent electrodes, J. Clean. Prod. 132 (20) (2016) 289–297.
[9] G. Berckmans, M. Messagie, J. Smekens, N. Omar, L. Vanhaverbeke, J.V. Mierlo, Cost projection of state of the art lithium-ion batteries for electric vehicles up to 2030, Energies 10 (2017) 1314, https://doi.org/10.3390/en10091314.
[10] H.D. Yoo, G. Salitra, D. Sharon, D. Aurbach, On the challenge of developing advanced technologies for electrochemical energy storage and conversion, Mater. Today 17 (3) (2014) 110–121.
[11] G.P. Hammond, T. Hazeldine, Indicative energy technology assessment of advanced rechargeable batteries, Appl. Energy 138 (15) (2015) 559–571.
[12] X. Su, Q. Wu, J. Li, X. Xiao, A. Lott, W. Lu, B.W. Sheldon, J. Wu, Silicon-based nanomaterials for lithium-ion batteries: a review, Adv. Energy Mater. 4 (2014), 1300882.
[13] P.G. Bruce, S.A. Freunberger, L.J. Hardwick, J.-M. Tarascon, LiO_2 and Li-S batteries with high energy storage, Nat. Mater. 11 (2012) 19–29.
[14] N. Liu, H. Wu, M.T. McDowell, Y. Yao, C. Wang, Y. Cui, A yolk-shell design for stabilized and scalable Li-ion battery alloy anodes, Nano Lett. 12 (2012) 3315–3321.
[15] L.-F. Cui, R. Ruffo, C.K. Chan, H. Peng, Y. Cui, Crystalline amorphous core-shell silicon nanowires for high capacity and high current battery electrodes, Nano Lett. 9 (2009) 491–495.
[16] C.-M. Park, J.-H. Kim, H. Kim, H.-J. Sohn, Li-alloy based anode materials for Li secondary batteries, Chem. Soc. Rev. 39 (2010) 3115–3141.
[17] J.-M. Tarascon, M. Armand, Issues and challenges facing rechargeable lithium batteries, Nature 414 (2001) 359–367.
[18] J. Wen, Y. Yu, C. Chen, A review on lithium-ion batteries safety issues: existing problems and possible solutions, Mater. Express 2 (2012) 197–212.
[19] R. Chen, R. Luo, Y. Huang, F. Wu, L. Li, Advanced high energy density secondary batteries with multi-electron reaction materials, Adv. Sci. (Weinh). 3 (10) (2016), 1600051, https://doi.org/10.1002/advs.201600051.
[20] J. Ortega, R. Dueber, Energy density comparison of silver-zinc button cells with rechargeable Li-Ion and Li-Polymer coin and miniature prismatic cells, Battery Power 19 (4) (2015). www.BatteryPowerOnline.com.

[21] F. Wang, X. Wu, C. Li, Y. Zhu, L. Fu, Y. Wu, X. Liu, Nanostructured positive electrode materials for post-lithium ion batteries, Energy Environ. Sci. 9 (2016) 3570–3611.
[22] J.O. GilPosada, A.J.R. Rennie, S.P. Villar, V.L. Martins, J. Marinaccio, C.F. Glover, D.A. Worsley, P.J. Hall, Aqueous batteries as grid scale energy storage solutions, Renew. Sustain. Energy Rev. 68 (2) (2017) 1174–1182.
[23] O. Mao, R.A. Dunlap, J.R. Dahn, Mechanically alloyed Sn-Fe(-C) powders as anode materials for Li-Ion batteries I. The Sn_2Fe-C system, J. Electrochem. Soc. 146 (2) (1999) 405–413.
[24] M. Wetjen, D. Pritzl, R. Jung, S. Solchenbach, R. Ghadimi, H.A. Gasteiger, Differentiating the degradation phenomena in silicon-graphite electrodes for lithium-ion batteries, J. Electrochem. Soc. 164 (12) (2017) A2840–A2852, https://doi.org/10.1149/2.1921712jes.
[25] Y. Jeon, H.K. Noh, H.-K. Song, A lithium-ion battery using partially lithiated graphite anode and amphi-redox $LiMn_2O_4$ cathode, Sci. Rep. 7 (1) (2017) 14879, https://doi.org/10.1038/s41598-017-14741-x.
[26] S. Goriparti, E. Miele, F.D. Angelis, E.D. Fabrizio, R.P. Zaccaria, C. Capiglia, Review on recent progress of nanostructured anode materials for Li-ion batteries, J. Power Sources 257 (2014) 421–443.
[27] A. Gupta, S.R. Dhakate, P. Gurunathan, K. Ramesha, High rate capability and cyclic stability of hierarchically porous Tin oxide (IV)–carbon nanofibers as anode in lithium ion batteries, Appl. Nanosci. 7 (2017) 449–462.
[28] W. Li, J. Zheng, T. Chen, T. Wang, X. Wang, X. Li, One step preparation of a high-performance Ge–C nanocomposite anode for lithium ion batteries by tandem plasma reactions, Chem. Commun. 50 (2014) 2052, https://doi.org/10.1039/C3CC47719C.
[29] C. Nithya, S. Gopukumar, rGO/nano Sb composite: a high-performance anode material for Na^+ ion batteries and evidence for the formation of nanoribbons from the nano rGO sheet during galvanostatic cycling, J. Mater. Chem. A 2 (2014) 10516.
[30] A. Civera, M. Pavese, G. Saracco, V. Specchia, Combustion synthesis of perovskite-type catalysts for natural gas combustion, Catal. Today 83 (15) (2003) 199–211.
[31] K.M. Parida, K.H. Reddy, S. Martha, D.P. Das, N. Biswal, Fabrication of nanocrystalline $LaFeO_3$: an efficient sol–gel auto-combustion assisted visible light responsive photocatalyst for water decomposition, Int. J. Hydrogen Energy 35 (22) (2010) 12161–12168.
[32] M. A. Carpenter, S. M. A. Kolmakov, Metal Oxide Nanomaterials for Chemical Sensors, Integrated Analytical Systems, Springer, New York, pp 1-559. DOI 10.1007/978-1-4614-5395-6.
[33] J. Zhu, H. Li, L. Zhong, P. Xiao, X. Xu, X. Yang, Z. Zhao, J. Li, Perovskite oxides: preparation, characterizations, and applications in heterogeneous catalysis, ACS Catal. 4 (9) (2014) 2917–2940, https://doi.org/10.1021/cs500606g.
[34] A. Grimaud, K.J. May, C.E. Carlton, Y.–L. Lee, M. Risch, W.T. Hong, J. Zhou, Y. Shao-Horn, Double perovskites as a family of highly active catalysts for oxygen evolution in alkaline solution, Nat. Commun. 4 (2013) 2439, https://doi.org/10.1038/ncomms3439.
[35] E. Fabbri, A. Habereder, K. Waltar, R. Kötz, T.J. Schmidt, Developments and perspectives of oxide-based catalysts for the oxygen evolution reaction, Catal. Sci. Technol. 4 (2014) 3800–3821, https://doi.org/10.1039/C4CY00669K.
[36] M.R. Mullen, J.V. Spirig, J. Hoy, J.L. Routbort, D. Singh, P.K. Dutta, Development of nanosized lanthanum strontium aluminum manganite as electrodes for potentiometric oxygen sensor, Sens. Actuators B Chem. 203 (2014) 670–676.
[37] R. Nechache, C. Harnagea, S. Li, L. Cardenas, W. Huang, J. Chakrabartty, F. Rosei, Bandgap tuning of multiferroic oxide solar cells, Nat. Photon. 9 (2015) 61–67.
[38] W. Wang, M.O. Tade, Z. Shao, Research progress of perovskite materials in photocatalysis- and photovoltaics-related energy conversion and environmental treatment, Chem. Soc. Rev. 44 (2015) 5371–5408.
[39] C. Ji, Z. Sun, A. Zeb, S. Liu, J. Zhang, M. Hong, J. Luo, Bandgap narrowing of lead-free perovskite-type hybrids for visible-light-absorbing ferroelectric semiconductors, J. Phys. Chem. Lett. 8 (9) (2017) 2012–2018, https://doi.org/10.1021/acs.jpclett.7b00673.
[40] Z. Fan, K. Sun, J. Wang, Perovskites for photovoltaics: a combined review of organic–inorganic halide perovskites and ferroelectric oxide perovskites, J. Mater. Chem. A 3 (2015) 18809–18828, https://doi.org/10.1039/c5ta04235f.
[41] M.V. Reddy, G.V.S. Rao, B.V.R. Chowdari, Metal oxides and oxysalts as anode materials for Li ion batteries, Chem. Rev. 113 (7) (2013) 5364–5457, https://doi.org/10.1021/cr3001884.
[42] Z.–L. Wang, D. Xu, J.-J. Xu, X.-B. Zhang, Oxygen electrocatalysts in metal–air batteries: from aqueous to nonaqueous electrolytes, Chem. Soc. Rev. 43 (2014) 7746–7786.
[43] J. Sunarso, S.S. Hashim, N. Zhu, W. Zhou, Perovskite oxides applications in high temperature oxygen separation, solid oxide fuel cell and membrane reactor: a review, Prog. Energy Combust. Sci. 61 (2017) 57–77.
[44] M.D. Luu, N.N. Dao, D.V. Nguyen, N.C. Pham, T.N. Vu, T.D. Doan, A new perovskite-type $NdFeO_3$ adsorbent: synthesis, characterization, and As(V) adsorption, Adv. Nat. Sci. Nanosci. Nanotechnol. 7 (2016), 025015.
[45] S. Yu, K. Yao, F.E.H. Tay, Structure and properties of $(1-x)(0.6Pb(Zn1/_3Nb_{2/3})O_{3-0.4}Pb(Mg_{1/3}Nb_{2/3})O_3)_{-x}PbTiO_3$ thin films with perovskite phase promoted by polyethylene glycol, J. Sol Gel Sci. Technol. 42 (2007) 357–364, https://doi.org/10.1007/s10971-007-0744-6.
[46] I.A. Abdel-Latif, A.A. Ismail, H. Bouzid, A. Al-Hajry, Synthesis of novel perovskite crystal structure phase of strontium doped rare earth manganites using sol gel method, J. Magn. Magn. Mater. 393 (1) (2015) 233–238.
[47] A. Worayingyong, P. Kangvansura, S. Kityakarn, Schiff base complex sol–gel method for $LaCoO_3$ perovskite preparation with high-adsorbed oxygen, Colloids Surf. A Physicochem. Eng. Asp. 320 (1–3) (2008) 123–129.
[48] B. An, K. Cheng, C. Wang, Y. Wang, W. Lin, Pyrolysis of metal–organic frameworks to Fe_3O_4@Fe_5C_2 core–shell nanoparticles for Fischer–Tropsch synthesis, ACS Catal. 6 (6) (2016) 3610–3618, https://doi.org/10.1021/acscatal.6b00464.
[49] H. Yu, S. Ouyang, S. Yan, Z. Li, T. Yu, Z. Zou, Sol–gel hydrothermal synthesis of visible-light-driven Cr-doped $SrTiO_3$ for efficient hydrogen production, J. Mater. Chem. 21 (2011) 11347–11351.
[50] X. Jia, L. Shen, Y. Liu, W. Yu, X. Gao, Y. Song, W. Guo, S. Ruan, W. Chen, Performance improvement of inverted polymer solar cells thermally evaporating CuI as an anode buffer layer, Synth. Met. 198 (2014) 1–5.
[51] C.-C. Yang, Y.–X. Wang, Preparation of high performance $LiFePO_4$/C cathode materials by using polymer templates, Energy Procedia 61 (2014) 1417–1423.
[52] T.V.S.L. Satyavani, A.S. Kumar, P.S.V.S. Rao, Methods of synthesis and performance improvement of lithium iron phosphate for high rate Li-ion batteries: a review, Eng. Sci. Technol. Int. J. 19 (1) (2016) 178–188.
[53] Z. Xing, Z. Ju, J. Yang, H. Xu, Y. Qian, One-step solid state reaction to selectively fabricate cubic and tetragonal $CuFe_2O_4$ anode material for high power lithium ion batteries, Electrochim. Acta. 102 (2013) 51–57.
[54] L. Luo, R. Cui, H. Qiao, K. Chen, Y. Fei, D. Li, Z. Pang, K. Liu, Q. Wei, High lithium electroactivity of electrospun $CuFe_2O_4$ nanofibers as anode material for lithium-ion batteries, Electrochim. Acta 144 (2014) 85–91.
[55] M.V. Reddy, B.L.W. Wen, K.P. Loh, B.V.R. Chowdari, Energy storage studies on $InVO_4$ as high-performance anode material for Li-Ion batteries, ACS Appl. Mater. Interfaces. 5 (2013) 7777–7785.
[56] F. Zhou, P. Zhu, X. Fu, R. Chen, Rong Sun, Ching-ping Wong, Comparative study of LiMnPO4 cathode materials synthesized by solvothermal methods using different manganese salts, Cryst. Eng. Comm. 16 (2014) 766–774.
[57] I.R. Ahmad, M.J. Akhtar, M. Younas, M.J. Akhtar, M. ul Hassan, Small polaronic hole hopping mechanism and Maxwell-Wagner relaxation in $NdFeO_3$, J. Appl. Phys. 112 (7) (2012), 074105, https://doi.org/10.1063/1.4754866.